Supporting Information:

Nonadiabatic excited-state dynamics of ReCl(CO)$_3$(bpy) in two different solvents

Adam Šrut,[a,b] Sebastian Mai,[c] Igor V. Sazanovich,[d]

Jan Heyda,*[,a,b] Antonín Vlček,[a,e] Leticia González*[,c] and Stanislav Záliš*[,a]

September 20, 2022

[a] J. Heyrovský Institute of Physical Chemistry, Academy of Sciences of the Czech Republic, 182 23 Prague, Czech Republic. Tel: +420 26605 3268; E-mail: stanislav.zalis@jh-inst.cas.cz
[b] Department of Physical Chemistry, University of Chemistry and Technology, Prague, 166 28 Prague, Czech Republic. Tel: +420 22044 4297; E-mail: jan.heyda@vscht.cz
[c] Institute for Theoretical Chemistry, University of Vienna, Währinger Straße 17, 1090 Vienna, Austria. Tel: +43 1 4277 52750; E-mail: leticia.gonzalez@univie.ac.at
[d] Central Laser Facility, Research Complex at Harwell, STFC, Rutherford Appleton Laboratory, Harwell Oxford, Didcot, Oxfordshire, OX11 0QX, United Kingdom.
[e] Department of Chemistry, Queen Mary University of London, London E1 4NS, United Kingdom.

S.1 Solvent parameterization and Temperature effects

S.1.1 Solvent parameterization

Rebpy intramolecular geometry corresponding to the ground-state energetic minimum in vacuum was fixed during classical simulations. Nonbonding interactions were determined from a generalized Amber force-field (GAFF) and partial charges were taken from a Mulliken population analysis. Solvent molecules were parametrized by the recommended protocol,[1,2] i.e., GAFF was used for bonded and nonbonded interactions, and partial charges were determined via restricted electrostatic potential fitting procedure (RESP). Resulting charges for ACN and DMSO are depicted in Figure S1.

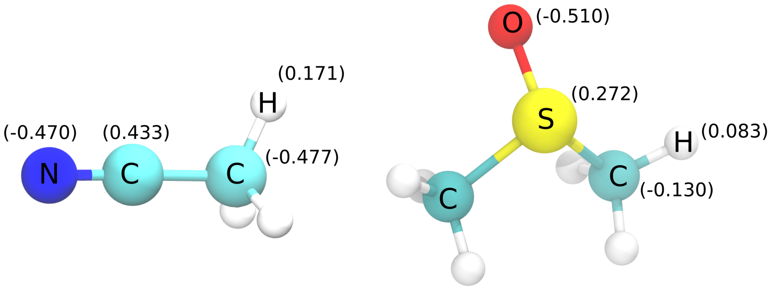

Figure S1: ACN and DMSO molecules with partial charges (in a.u.) used for simulations presented in this work.

S.1.2 Temperature effects

The temperature was taken into account in the preparation of the initial conditions, as the system was first equilibrated at room temperature, 300 K (Figure 1). We are aware that sampling of the initial conditions at different temperatures could lead to population of different excited states and thus to different ISC pathways[3] but no relevant experimental data are available. Therefore, we have run all simulations at a single temperature of 300 K that closely resembles realistic conditions. Accordingly, the non-adiabatic simulation should resemble the realistic conditions, even if not completely. We are aware that the redistribution of the excess kinetic energy that the system gains by relaxing to the lower excited states is not described faithfully. First, surface-hopping simulations suffer from zero-point energy leakage,[4] i.e., the kinetic energy will flow from the high frequency modes to the low frequency ones. Second, within the QMMM model, the excess kinetic energy cannot be redistributed to the solvent since the wavefunction of the solvent environment is not present in the simulations.

S.2 Excited states

The absorption spectrum and the density of states from the initial conditions was simulated by broadening the discrete spectrum with a Gaussian kernel of a 0.1 eV width:

$$\sigma(E) = \left[\sum_{j=1}^{N_{\text{inits}}} \sum_{i=1}^{N_{\text{states}}} f_{ij} \cdot \delta(E - E_{ij})\right] \otimes \exp\left(-\frac{E^2}{(0.6 \cdot 0.1\,\text{eV})^2}\right) \tag{1}$$

where f_{ij} and E_{ij} being the oscillator strength and excitation energy for j-th initial condition and i-th excited state, respectively. δ is the Dirac-delta function.

Figure S2 compares the density of states in **Rebpy** as computed by spin-free TD-DFT in ACN and DMSO solvent from ca 500 initial conditions extracted from the QM/MM trajectories. Densities of low-lying singlet (S_1–S_3) and triplet (T_1–T_4) states exhibit a bit broader distribution in DMSO than in ACN. Non-adiabatic simulations in both solvents,DMSO and ACN, were carried out with the lowest 6 singlet and 5 triplet states.

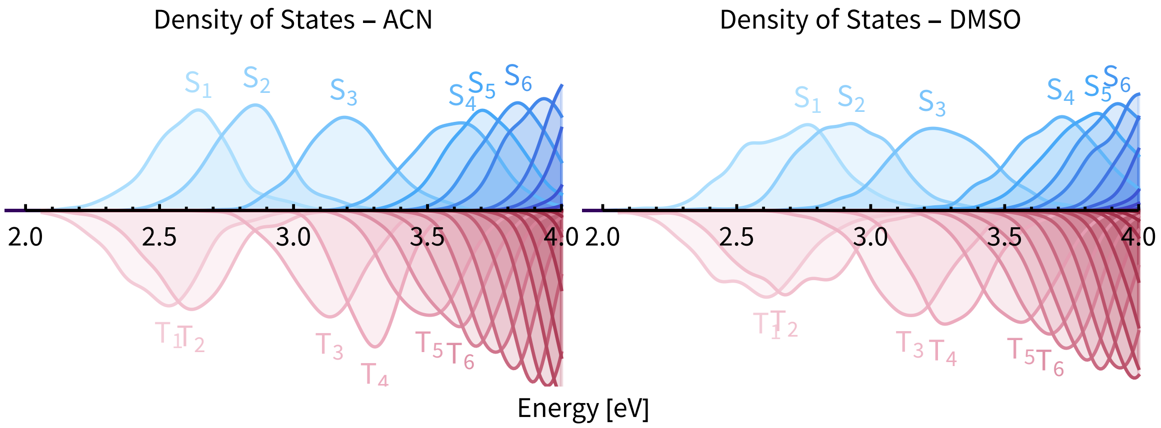

Figure S2: Density of states for initial conditions for simulations in ACN (left) and DMSO (right). 20 singlet and 20 triplet states are plotted, but only lowest six states are labelled since they contribute to the energy region of interest. The histograms were smoothed by convolution with a Gaussian kernel of a 0.1 eV width.

In order to explore the characters of states at time zero and also the charge redistribution within **Rebpy** after vertical excitation a charge transfer analysis was carried out utilizing the procedures implemented in the TheoDORE package.[5] Figure S3 depicts characters of low-lying singlet and triplet states computed from the initial conditions for non-adiabatic simulations in ACN and DMSO. Excited states that are vastly populated in non-adiabatic dynamic simulations (S_1, S_2, T_1, T_2 and T_3 as depicted in Figure 5) have a predominant $Re(CO)_3 \rightarrow$ bpy MLCT character mixed with about 20 % of Cl → bpy LLCT. Noticeable differences between solvents can be spotted for T_3 and T_4, these states also exhibit much higher bpy → bpy IL character than the other triplet or singlet states.

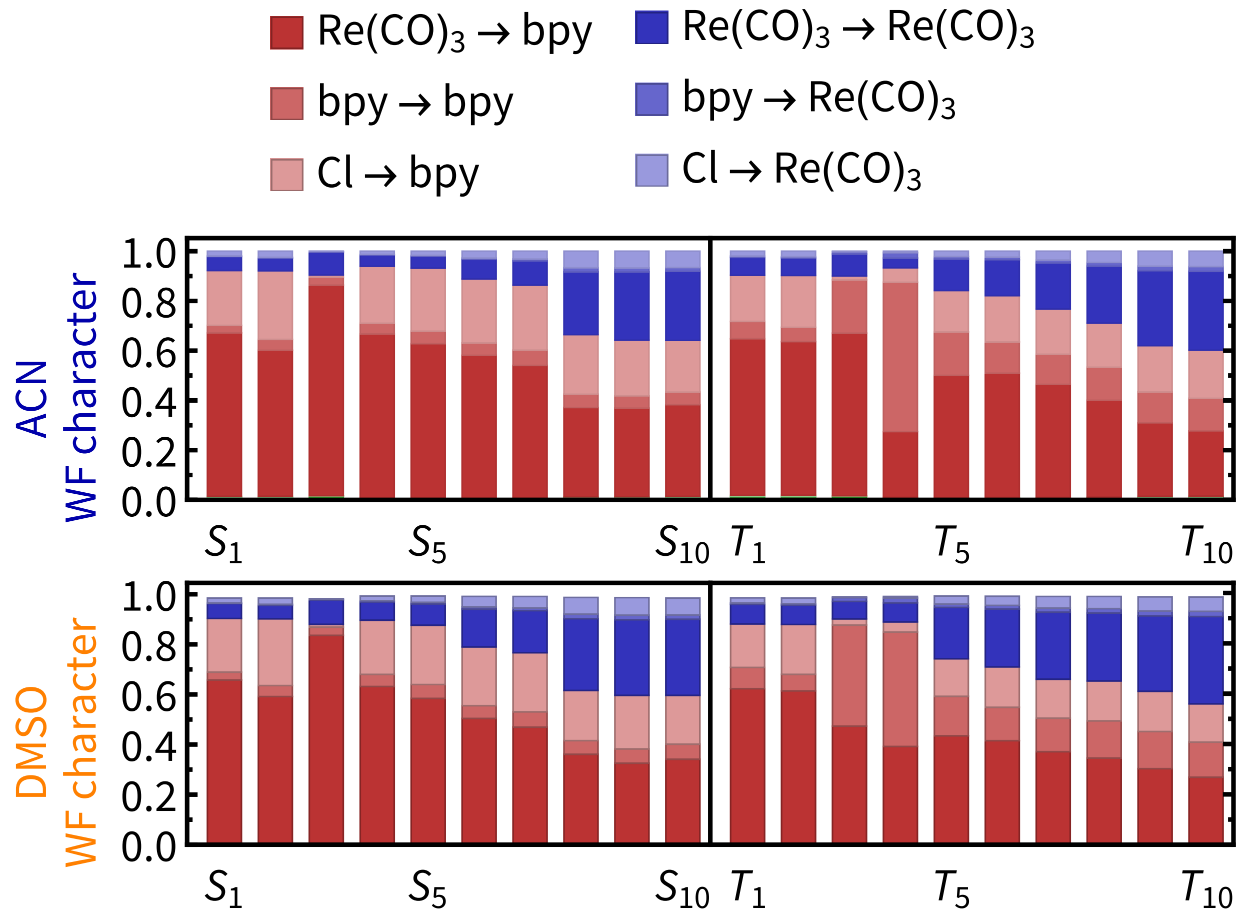

Figure S3: Wavefunction character for the lowest 10 singlet and 10 triplet states of **Rebpy** in ACN (upper panels) and DMSO (lower panels) solvents. Data are averaged over 492 and 541 uncorrelated snapshots in ACN and DMSO solvent, respectively. Note that charge transfers to Cl ligand (level of green) have almost zero contribution to the wavefunction character and therefore they are not visible in plots.

S.3 Frozen-nuclei dynamics

The total electronic wavefunction of one trajectory can be written as a superposition of spin-mixed states:[6]

$$|\Psi\rangle = \sum_{i=1}^{N_{\mathrm{states}}} c_i^{\mathrm{spin-mixed}} \left|\psi_i^{\mathrm{spin-mixed}}\right\rangle \tag{2}$$

coefficients $c_i^{\mathrm{spin-mixed}}$ can be then expressed as:

$$\begin{aligned} c_i^{\mathrm{spin-mixed}} &= \left\langle \Psi \middle| \psi_i^{\mathrm{spin-mixed}} \right\rangle && \text{(3a)} \\ &= \sum_{j=1}^{N_{\mathrm{states}}} \left\langle \Psi \middle| \psi_j^{\mathrm{spin-free}} \right\rangle \left\langle \psi_j^{\mathrm{spin-free}} \middle| \psi_i^{\mathrm{spin-mixed}} \right\rangle && \text{(3b)} \\ &= \sum_{j=1}^{N_{\mathrm{states}}} c_j^{\mathrm{spin-free}} \cdot U_{ji} && \text{(3c)} \end{aligned}$$

In Equation 3b, the resolution of identity was employed. Resulting Equation 3c gives a prescription for the transformation between spin-mixed and spin-free bases. Matrix **U** is a so-called transformation matrix, properly defined in Ref. [6].

Frozen-nuclei dynamics were performed in order to show the consistency of our results with Ref. [7]. In this set of simulations, all atomic nuclei were frozen and only the electronic wavefunction could evolve in time according to:

$$\mathbf{c}^{\mathrm{spin-free}}(t) = \exp\left(-\frac{i}{\hbar} t \mathbf{H}^{\mathrm{tot}}\right) \mathbf{c}^{\mathrm{spin-free}}(0) \tag{4}$$

where $\mathbf{c}^{\mathrm{spin-free}}$(t) are coefficients of spin-free states at time t, and $\mathbf{H}^{\mathrm{tot}}$ is the matrix representation of the total Hamiltonian in spin-free basis, with off-diagonal elements of $\mathbf{H}^{\mathrm{tot}}$ being spin-orbit couplings between spin-free states. The $\mathbf{c}^{\mathrm{spin-free}}(0)$ vector has a non-zero value only for initially populated singlet states (S_1 and S_2), hence the initial electronic population is in the singlet states (see Methods).

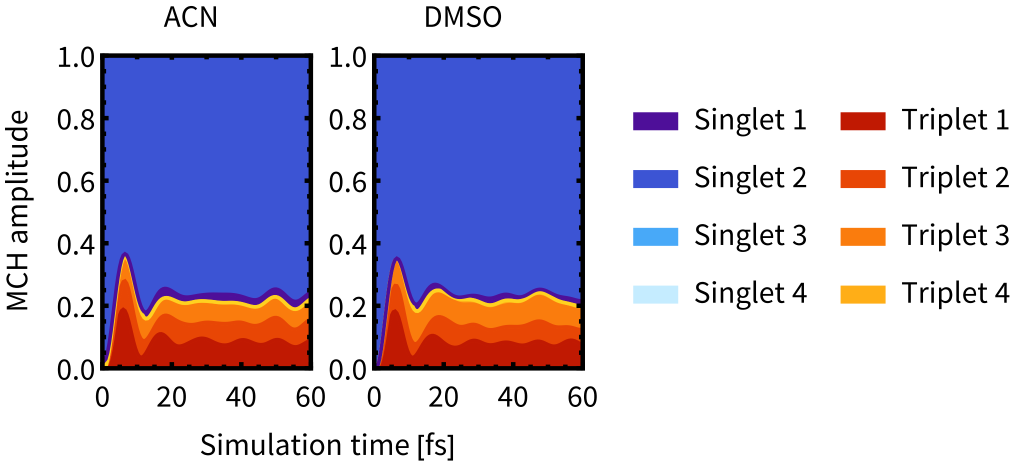

Figure S4: Temporal evolution of spin-free states population (averaged over an ensemble of trajectories) in frozen nuclei dynamics depicted as a stacked plot. 4 singlet and 4 triplet states out of 20 singlet and 20 triplet states considered in the simulations are plotted. Molecular Coulomb Hamiltonian (MCH) amplitude corresponds to the projection of a spin-free state to the total electronic wavefunction, i.e., MCH amplitude = $\left|c_i^{\mathrm{spin-free}}\right|^2$.

S.4 Character of the electronic wavefunction

The charge transfer numbers[8] were computed on-the-fly for each spin-free state in non-adiabatic simulations. **Rebpy** was partitioned into 3 fragments, namely: bpy, Cl and Re(CO)$_3$, in total leading to 9 charge transfer numbers. The character of the total wavefunction is determined via eq.(5a), (5b), employing the weights of the spin-free populations:

$$\Omega_{AB} = \frac{1}{N_{\text{trajs}}} \sum_{n=1}^{N_{\text{trajs}}} \sum_{i=1}^{N_{\text{states}}} \left| c_{i,n}^{\text{spin-free}} \right|^2 \Omega_{AB,i,n} \tag{5a}$$

$$= \frac{1}{N_{\text{trajs}}} \sum_{n=1}^{N_{\text{trajs}}} \sum_{i=1}^{N_{\text{states}}} \left| \sum_{j=1}^{N_{\text{states}}} U_{ij,n} c_{j,n}^{\text{spin-mixed}} \right|^2 \Omega_{AB,i,n} \tag{5b}$$

where $\Omega_{AB,i}$ is a charge transfer number from fragment A to fragment B for spin-free state i. Figure S3 depicts the character of electronic wavefunction in terms of charge transfer numbers. The Re(CO)$_3$ → bpy MLCT character is strongly mixed with Cl → bpy LLCT, whose contribution slightly decreases during nonadiabatic simulations. No significant differences between the two solvents were observed.

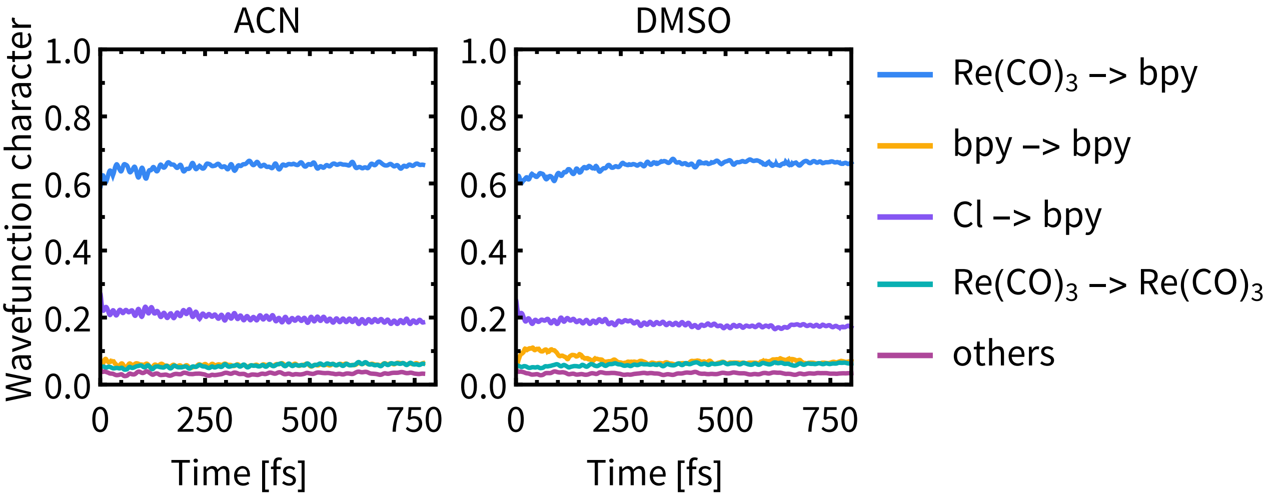

Figure S5: Temporal evolution of the wavefunction character in terms of charge transfer numbers between three fragments (bpy, Cl and Re(CO)$_3$) in **Rebpy** complex.

Figures S6 and S7 omit the averaging over trajectories and show the wavefunction character as a histogram for distinct time windows during simulations. Cl → bpy LLCT and Re(CO)$_3$ → bpy MLCT characters exhibit distributions with two maxima. This points to a presence of two groups of trajectories with vastly different wavefunction character. The first group is predominantly populated and average wavefunction characters fit to the situation presented in Figure S5. The second group has a much smaller Cl → bpy LLCT but a higher Re(CO)$_3$ → bpy MLCT character and is populated much less.

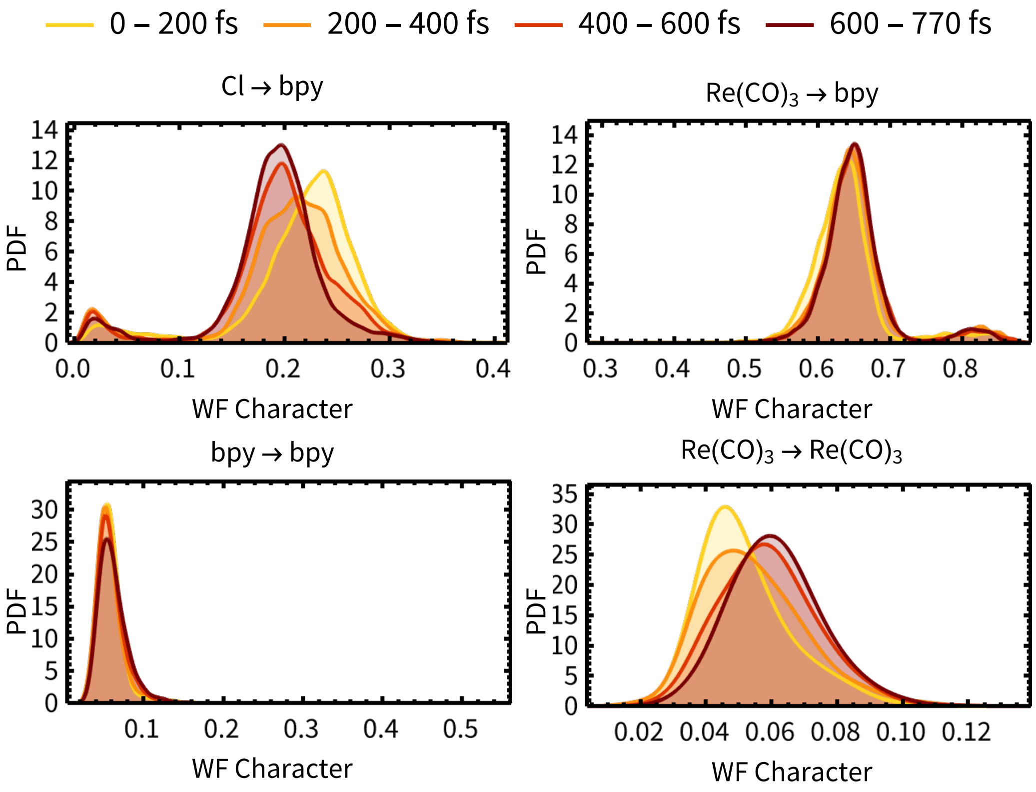

Figure S6: Histograms of important wavefunction characters for distinct time windows, simulations in ACN. PDF = probability density function.

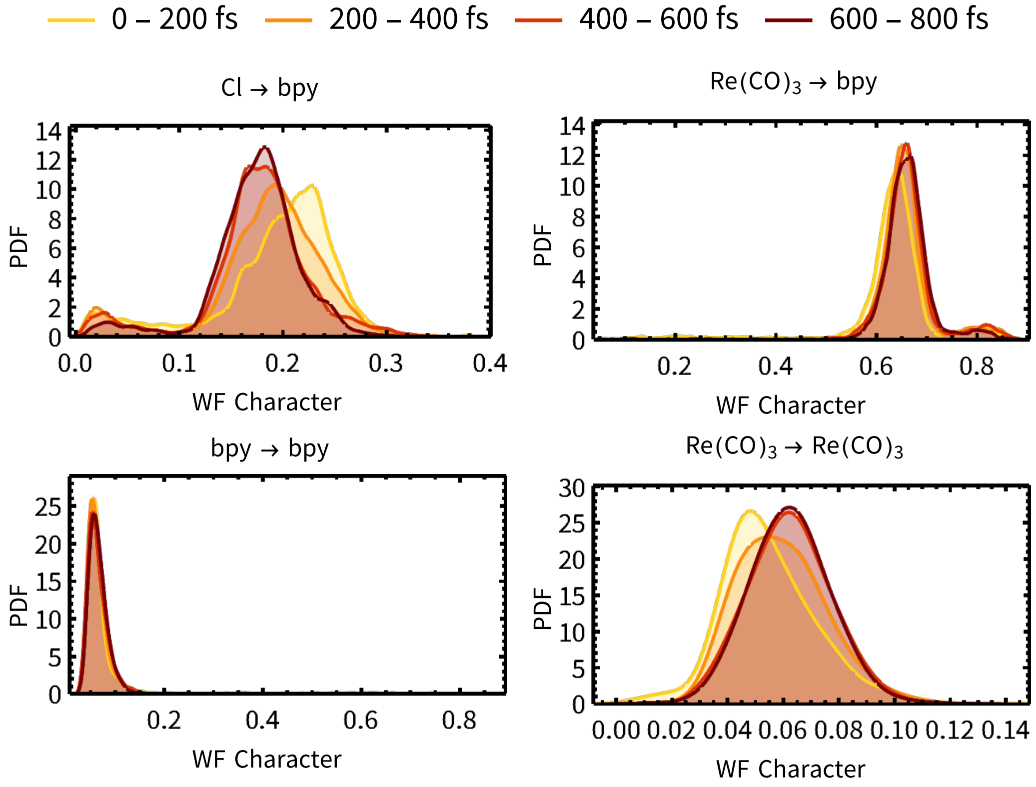

Figure S7: Histograms of important wavefunction characters for distinct time windows, simulations in DMSO. PDF = probability density function.

S.5 Time-resolved fluorescence spectra

Emission spectra were simulated by collecting energy differences and oscillator strengths between the active state and the ground state from all trajectories. The time-wavelength 2D discrete spectrum was then convoluted with two gaussian kernels: In the energy domain with a $0.5\,\mathrm{eV}$ fwhm to obtain continuous spectral bands and in the time domain with a width of $100\,\mathrm{fs}$ to simulate the experimental conditions. The whole procedure can be expressed as

$$I(E,t) = \left[\sum_{i=1}^{N_{\mathrm{trajs}}} (f_{\mathrm{Act.}\to\mathrm{GS}})_{i,t} \cdot \delta(E - E_{i,t})\right] \otimes \exp\left(-\frac{E^2}{(0.6 \cdot 0.5\,\mathrm{eV})^2}\right) \otimes \exp\left(-\frac{t^2}{(0.6 \cdot 100\,\mathrm{fs})^2}\right) \tag{6}$$

where $\delta(E)$ is the Dirac delta distribution and the factor 0.6 in Gaussian kernels converts a full-width at half maximum to the standard deviation. Symbol $\otimes$ is used to denote convolution.

Comparison of the simulated spectrum in ACN with the experimental one (Figure 6) shows an overall good agreement in both time and energy domains. Spectra exhibit an initial the maximum at 525 nm and evolve towards a decaying peak at approximately 600 nm. The persisting signal in the experimental spectrum on longer time scale ($t > 0.6\,\mathrm{ps}$) is assigned to phosphorescence from T_1 and presents only isolated events of photon detection. This rare event is observable only in the experiment, where $\approx 10^{20}$ molecules are excited.[9]

We note that the experimentally detected fluorescence was polarized parallel to the excitation (pump) beam polarization. Possible effects of time-dependent fluorescence anisotropy were neglected in both experimental data analysis as well as in present theoretical simulations where only absolute values of transition moments were considered.

S.6 Kinetics fitting

S.6.1 *Kinetics model for intersystem crossing dynamics*

We follow a kinetics model from Ref. [10], which is shown in Figure S8. First, total singlet population is divided into two subpopulations, S_{hot} and S_{cold}. Next, it is assumed that the triplet states can be reached either directly from S_{hot} (with time constant τ_{fast}) or indirectly through S_{cold} (with time constant τ_{slow}). A set of three resulting differential equations may be compactly written in a matrix form:

$$\frac{\mathrm{d}}{\mathrm{d}t}\begin{pmatrix} S_{\text{hot}}(t) \\ S_{\text{cold}}(t) \\ T(t) \end{pmatrix} = \begin{pmatrix} -\frac{1}{\tau'}-\frac{1}{\tau_1} & 0 & 0 \\ \frac{1}{\tau'} & -\frac{1}{\tau_2} & 0 \\ \frac{1}{\tau_1} & \frac{1}{\tau_2} & 0 \end{pmatrix}\begin{pmatrix} S_{\text{hot}}(t) \\ S_{\text{cold}}(t) \\ T(t) \end{pmatrix} \tag{7}$$

whose solution gives rise to a biexponential decay of the total singlet population:

$$S(t) = S_{\text{hot}}(t) + S_{\text{cold}}(t) = re^{-\frac{t}{\tau_{\text{fast}}}} + (1-r)e^{-\frac{t}{\tau_{\text{slow}}}} \tag{8a}$$

$$\tau_{\text{fast}} = \frac{1}{\frac{1}{\tau_1}+\frac{1}{\tau'}} \tag{8b}$$

$$\tau_{\text{slow}} = \tau_2 \tag{8c}$$

$$r = \frac{\frac{1}{\tau_1}}{\frac{1}{\tau_1}+\frac{1}{\tau'}-\frac{1}{\tau_2}} \tag{8d}$$

According to Equation (8a), the population flow is split into fast and slow channel characterised by time constants τ_{fast} and τ_{slow}, respectively. Parameter r in Equation (8d) determines the branching ratio of the two channels. Constant τ_2 has a negligible contribution to the value of r since it is assumed to be much larger than τ_1 and τ'.

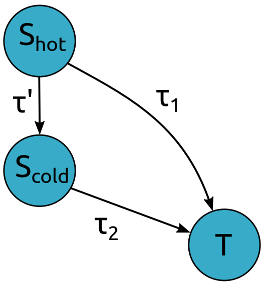

Figure S8: Schematic representation of proposed kinetic model.

S.6.2 Fluorescence decay

Assuming a biexponential fluorescence decay,[7,9,11] the equation used to fit the decay kinetics parameters has the form:

$$I(t) = A \int_0^{\infty} \left(re^{-\frac{t'}{\tau_1}} + (1-r)e^{-\frac{t'}{\tau_2}} \right) e^{-\left(\frac{t-t'}{0.6 \cdot 100\ \mathrm{fs}}\right)^2} \mathrm{d}t' \tag{9}$$

where the expression in the parentheses describes the biexponential decay with emission decay times, τ_1 and τ_2, and r defines the population branching ratio flow between the two channels. The whole expression is then convoluted with an instrument response function $\exp\left(-\left[\frac{t-t'}{0.6 \cdot 100\ \mathrm{fs}}\right]^2\right)$, 100 fs is the temporal resolution of experimental setup and 0.6 is a conversion factor between variance and full-width-at-half-maximum (FWHM). A is the overall intensity factor.

S.6.3 Error estimation

Error bars for the time constants for the fluorescence decay and the ISC rate were estimated by bootstrapping.[12] From the original ensemble of trajectories a set of new samples was obtained by stochatically replicating some trajectories and consequently also omitting some. The kinetic parameters are computed again for all resampled ensembles (100 were in this work) resulting in a statistical distribution of these parameters. The arithmetic standard deviations of of this distribution will then serve as an estimate of the uncertainty of a given kinetic parameter.

S.7 Average geometries of the main clusters

Figure S9 displays reference geometries, which were used to compute 2-dimensional temporal evolution of **Rebpy** geometrical relaxation by means of root-mean-square-deviation (RMSD) distance, in the two solvents (left panels of Figure 8). The average geometry of the main cluster in GS and in the near-equilibrium lowest excited state are shown in Figure S9. In each solvent, the two geometries are overlaid to highlight the differences. As the **Rebpy** geometry relaxes from the GS region of the geometrical space to the near-equilibrium excited-state region, the most significant change in geometry is the alignment of bipyridine ligand and equatorial CO ligands to a single common plane.

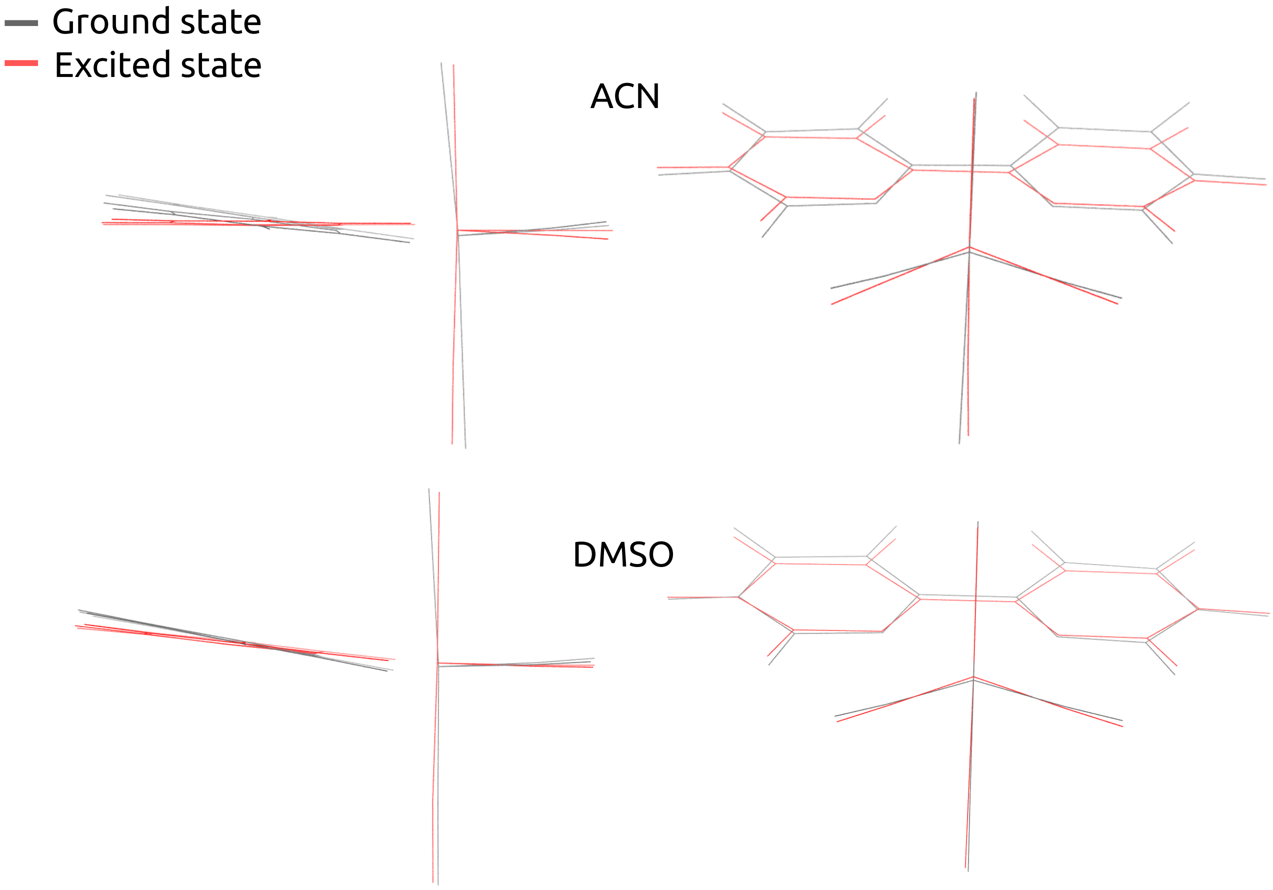

Figure S9: Comparison of average geometries of the main cluster of GS and the near-equilibrium lowest excited state. Left: Side views, Right: front views, Cl ligand at the bottom.

S.8 Proximal radial distribution function

Proximal radial distribution function was employed to describe a realistic solvent distribution around different regions (residues) of **Rebpy**. First, we define the conventional radial distribution function (RDF) and use it to illustrate the differences with the proximal radial distribution function (pRDF).

In MD simulations, the structure of the solvation environment in the vicinity of any molecule is usually described by a (pair) RDF. Let A be an atom of **Rebpy** complex and B an atom of a solvent molecule at a distance r_{AB}. The interpretation of RDF is intuitive, as it is a ratio between a local density of particle B at distance r_{AB}, $\rho_B(r_{AB})$, and its bulk density ρ_B^0. RDF is conveniently defined as:

$$g(r_{AB}) = \frac{\rho_B(r_{AB})}{\rho_B^0} = \frac{\Delta N_B(r_{AB})}{\rho_B^0 \Delta V(r_{AB})} \overset{\text{spherical}}{=} \frac{1}{\rho_B^0} \frac{\Delta N_B(r_{AB})}{4\pi r_{AB}^2 \Delta r} \tag{10}$$

where $\Delta N_B(r_{AB}) = N_B(r_{AB} + \Delta r) - N_B(r_{AB})$ represents the number of particles in a spherical layer of radius r_{AB} and thickness Δr. Analogously $\Delta V(r_{AB}) = 4\pi r_{AB}^2 \Delta r$ represents the volume of this spherical shell. Thus defined RDF exhibits sharp peaks (maxima, and minima) at short distances due to the interactions between atoms A, and B, and naturally converges to 1 when the two particles are far apart and their direct and indirect interactions vanish.

In contrast, large molecules of an irregular shape, such as organometallic complexes, proteins or polymers, are poorly represented by any single atom A or a point (typically a center of mass), which results in RDFs whose patterns are difficult to interpret. According to Lin and Pettitt,[13] RDF may significantly differ even for similarly solvated molecules when the distances are measured from solvent atoms to only one solute atom. To overcome this limitation, pRDF was proposed,[14] where the shortest distance between atoms of a solvent molecule and atoms of the solute is calculated, local density determined, and pRDF evaluated according to Eq. 10.

The advantages are clearly visible using the example of **Rebpy** in Figure S10. Solvation of **Rebpy** will be different around different ligands since **Rebpy** is not spherically symmetric and each ligand carries a different charge density distribution. Computation of pRDF provides a detailed insight into local solvation.

In Figure S10, we explain the algorithm of pRDF computation as used in this work. **Rebpy** is divided into a set of five residues, i.e. three carbonyl ligands, chlorine, and bipyridine, for which pRDFs are computed.

In the first step, the proximal volume ΔV needs to be calculated, which uniquely decomposes the space. For example, two equidistant surfaces are shown in Figure S10b, the closer silver surface measures the distance r from bipyridine and the further grey surface the distance $r + \Delta r$, hence the layer between surfaces of the same colour illustrates the volume element $\Delta V(r) = V(r + \Delta r) - V(r)$ of the respective residue. Next, we need to determine the number of solvent atoms

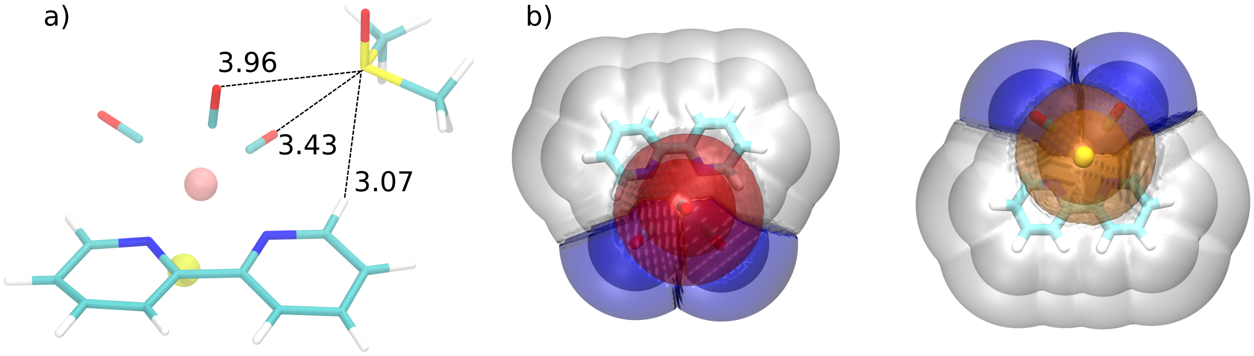

Figure S10: a) Example calculation of proximal distances (in Å) from S atom of DMSO to **Rebpy** ligands. b) Illustration of the proximal volume layers of **Rebpy** ligands used in computation of proximal radial distribution functions. Left: View from the top, right: view from the bottom. Equatorial carbonyls are depicted in blue, axial carbonyl in red, bipyridine in silver and chlorine in yellow.

of the same type in volume elements ΔV belonging to individual residues. To do so, distances to all **Rebpy** atoms have to be computed for each solvent atom and the closest one selected (see Figure S10a). Now, we have determined to which volume element and to which pRDF this solvent atom contributes. For example, the closest distances from a sulphur atom to three **Rebpy** residues (bipyridine, axial and equatorial carbonyl) are computed (Figure S10a). A sulphur atom contributes only to pRDF of the bipyridine ligand with a distance of 3.07 Å. By employing the same procedure for all DMSO molecules, and averaging over the trajectory, the number of DMSO molecules $\Delta N(r)$ in the proximal volume $\Delta V(r)$ is obtained and the local density and pRDF calculated according to Equation (10).

S.9 Spin-orbit couplings

The spin-orbit coupling matrix elements (SOCME) were extracted from the total Hamiltonian matrix in the spin-free basis. Resulting distributions with time resolution of 200 fs are then plotted in Figures 5, S11 and S13 for simulations in DMSO and ACN, respectively. Additionally, analysis of energy gaps between low-lying spin-free states was carried out, Figures S12 and S14).

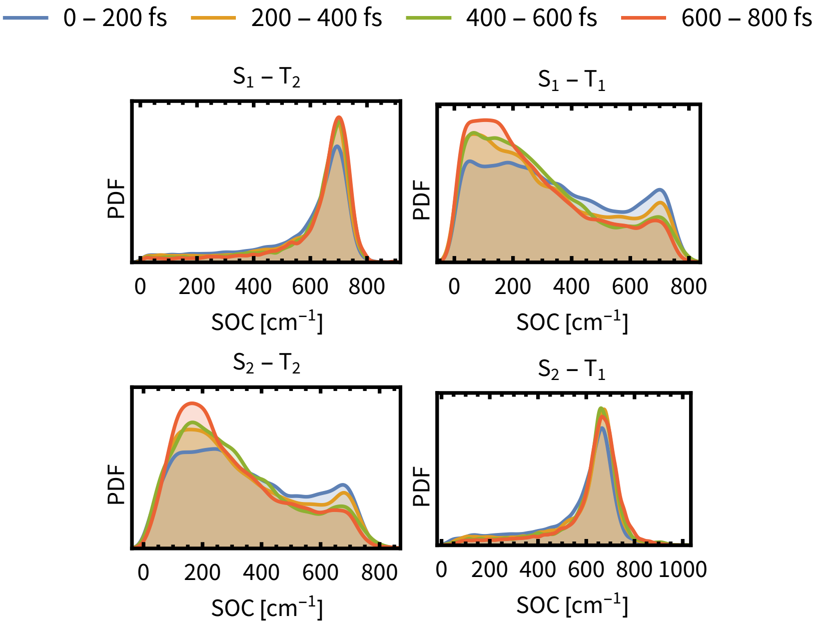

Figure S11: Time-dependent histograms of spin-orbit coupling (SOC) matrix elements for low-lying spin-free states of **Rebpy** in DMSO. PDF denotes probability density function.

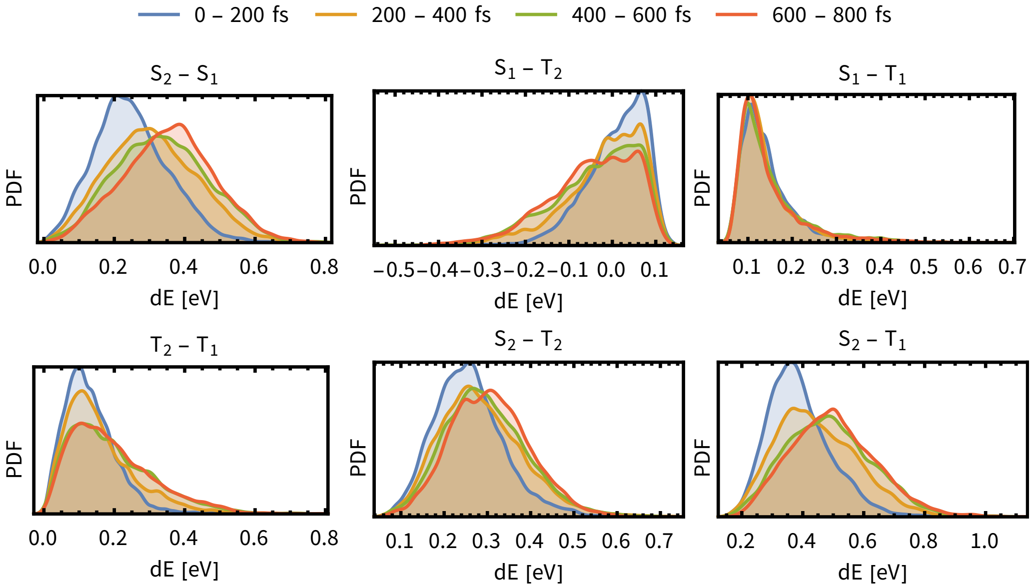

Figure S12: Time-dependent histograms of energy differences (dE) between low-lying spin-free states of **Rebpy** in DMSO. PDF denotes probability density function.

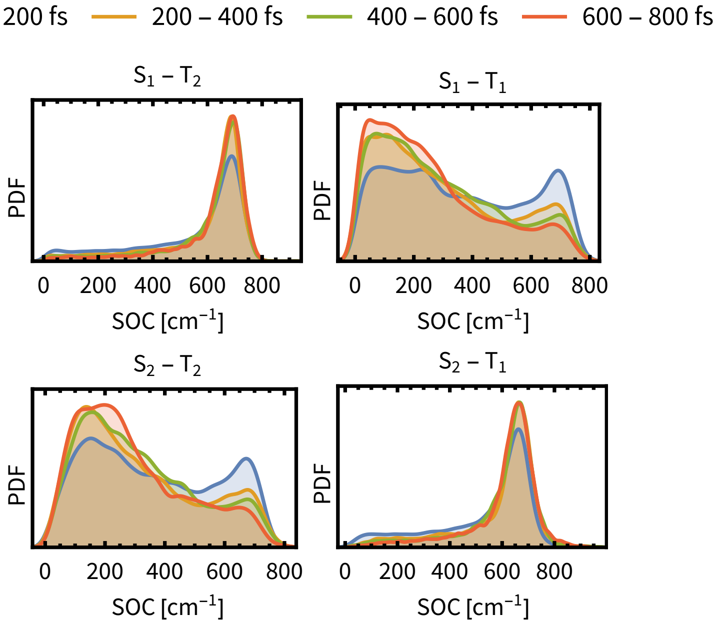

Figure S13: Time-dependent histograms of spin-orbit coupling (SOC) matrix elements for low-lying spin-free states of **Rebpy** in ACN. PDF denotes probability density function.

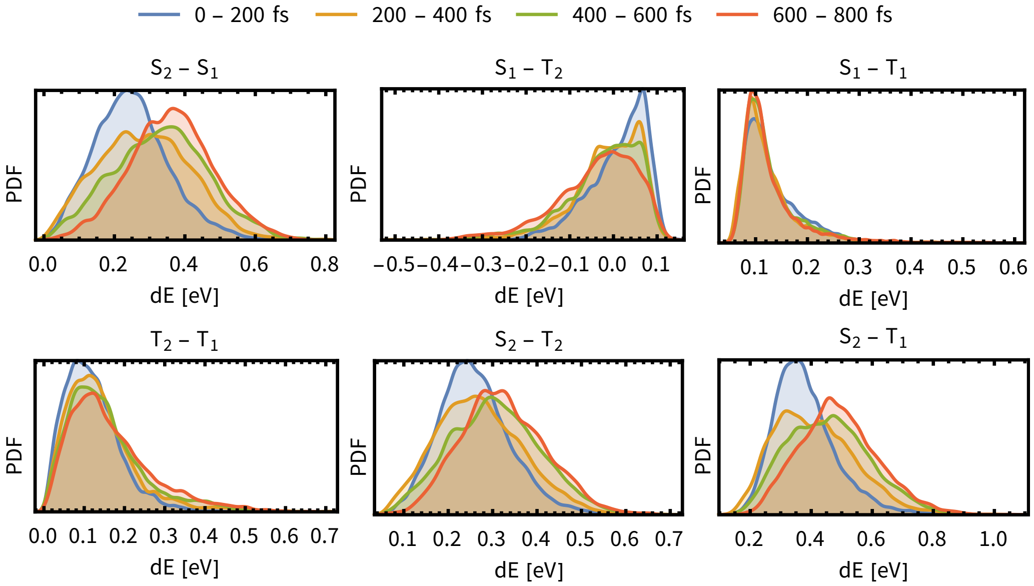

Figure S14: Time-dependent histograms of energy differences (dE) between low-lying spin-free states of **Rebpy** in ACN. PDF denotes probability density function.

S.10 Temporal evolution of spin-mixed states populations

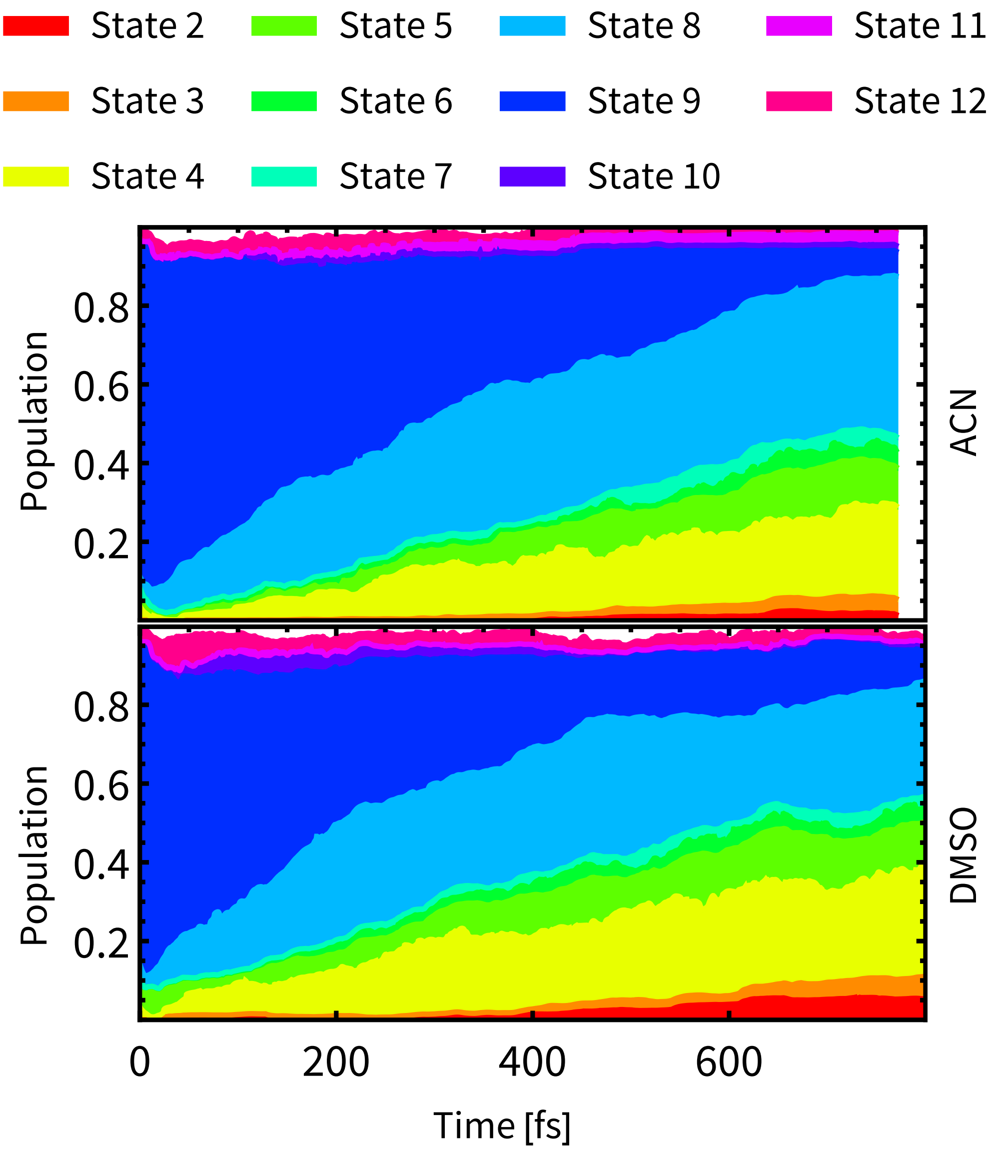

Figure S15: Stacked plot of temporal evolution of low-lying spin-mixed excited states (States 2-12, State 1 is GS), in which the non-adiabatic dynamics is practically realized. Temporal evolution in ACN and DMSO shown in the top and bottom panels respectively.

S.11 Temporal evolution of compositions of spin-mixed states

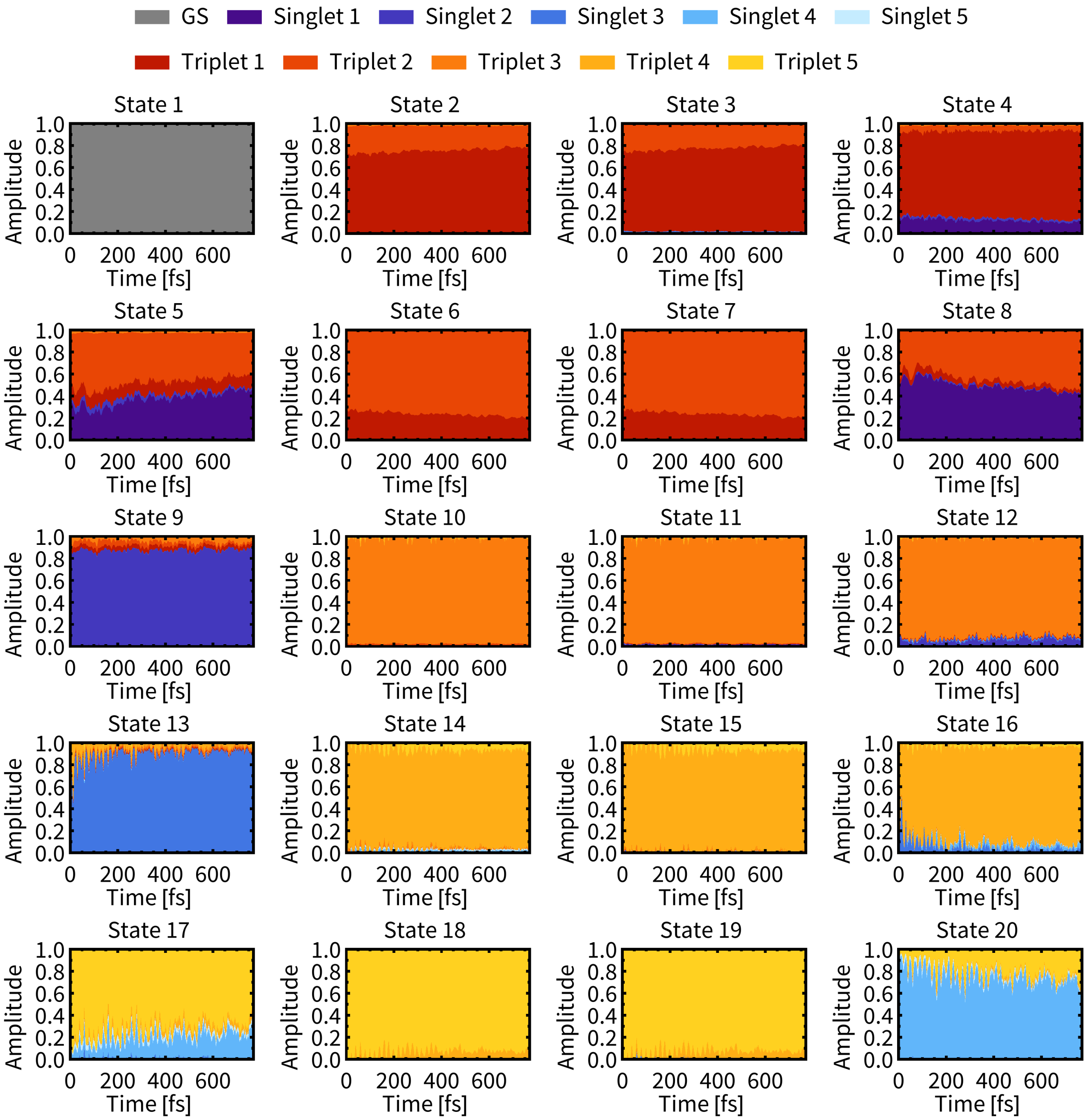

Figure S16: Temporal evolution of ensemble averaged composition of 20 spin-mixed states of **Rebpy** in ACN simulation set.

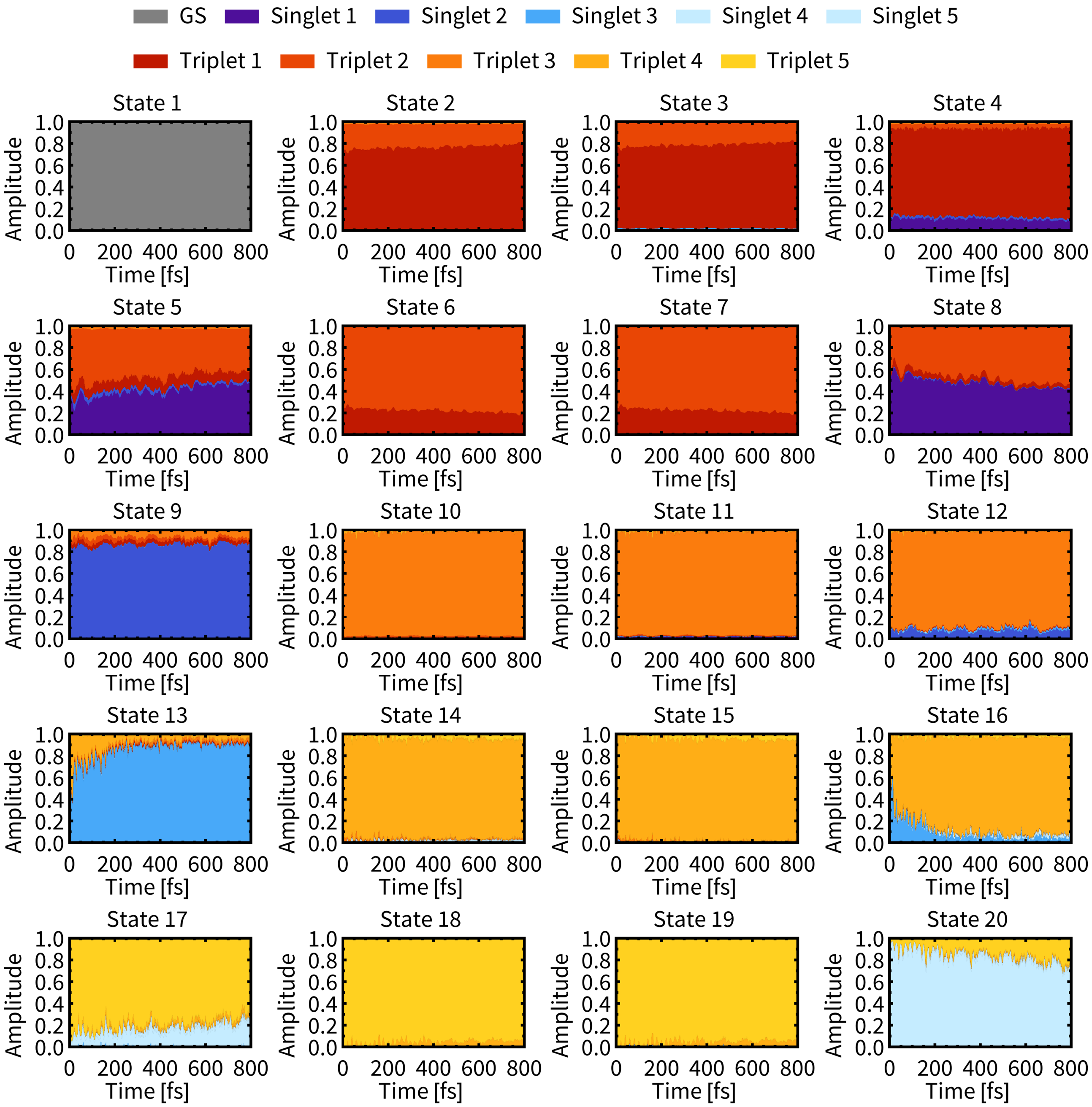

Figure S17: Temporal evolution of ensemble averaged composition of 20 spin-mixed states of **Rebpy** in DMSO simulation set.

S.12 Time resolved spectroscopy

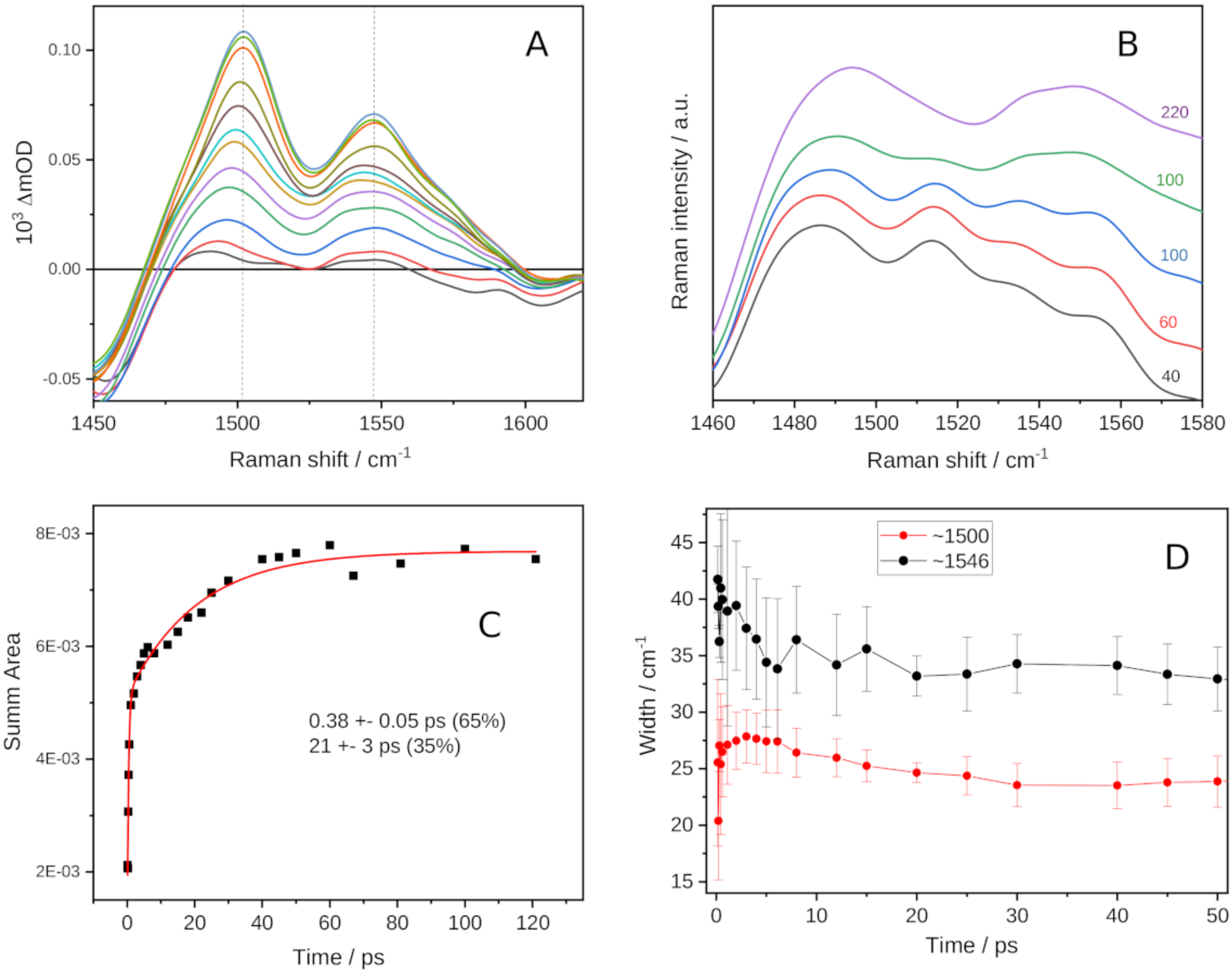

Figure S18: Dynamics of Raman bands in the 1450–1600 cm^{-1} range measured in CH$_3$CN. A: Time-resolved spectra adjusted to a common zero-signal level. Time delays from bottom up: 0.15, 0.20, 0.30, 0.45, 0.61, 1.1, 2.0, 6.1, 14.9, 30, 60, 122 ps. The dotted lines show band positions in the 60 ps spectrum. B: Detail of the spectral evolution from 40 to 220 fs; spectra are offset by a constant amount. C: Time-dependence of the sum of band areas in the 1450–1600 cm^{-1} range. D: Time-dependence of the widths (fwhm) of ~ 1500 and 1546 cm^{-1} Raman features. Band areas and widths were obtained by Gaussian decomposition. Reproduced with permission from ref. [15].

References

[1] J. Wang, R. M. Wolf, J. W. Caldwell, P. A. Kollman, and D. A. Case, *Journal of Computational Chemistry* **25**, 1157–1174 (2004).

[2] C. I. Bayly, P. Cieplak, W. D. Cornell, and P. A. Kollman, *Journal of Physical Chemistry* **97**, 10269–10280 (1993).

[3] J. P. Zobel, J. J. Nogueira, and L. González, *Physical Chemistry Chemical Physics* **21**, 13906–13915 (2019).

[4] S. Mukherjee and M. Barbatti, *Journal of Chemical Theory and Computation* **18**, 4109–4116 (2022).

[5] F. Plasser, *Journal of Chemical Physics* **152**, 84108 (2020).

[6] S. Mai, P. Marquetand, and L. González, *International Journal of Quantum Chemistry* **115**, 1215–1231 (2015).

[7] S. Mai and L. González, *Chemical Science* **10**, 10405–10411 (2019).

[8] S. Mai, F. Plasser, J. Dorn, M. Fumanal, C. Daniel, and L. González, *Coordination Chemistry Reviews* **361**, 74–97 (2018).

[9] A. Cannizzo, A. M. Blanco-Rodríguez, A. E. Nahhas, J. Šebera, S. Záliš, A. Vlček, and M. Chergui, *Journal of the American Chemical Society* **130**, 8967–8974 (2008).

[10] S. Mai, M. F. Menger, M. Marazzi, D. L. Stolba, A. Monari, and L. González, *Theoretical Chemistry Accounts* **139**, 65 (2020).

[11] A. El Nahhas, C. Consani, A. M. Blanco-Rodríguez, K. M. Lancaster, O. Braem, A. Cannizzo, M. Towrie, I. P. Clark, S. Záliš, M. Chergui, and A. Vlček, *Inorganic Chemistry* **50**, 2932–2943 (2011).

[12] *Sharc2.1: manual*, `https://sharc-md.org/?page_id=50#tth_sEc8.4` (visited on 09/06/2022).

[13] B. Lin and B. M. Pettitt, *Journal of Chemical Physics* **134**, 2011–2013 (2011).

[14] P. K. Mehrotra and D. L. Beveridge, *Journal of the American Chemical Society* **102**, 4287–4294 (1980).

[15] M. Pižl, A. Picchiotti, M. Rebarz, N. Lenngren, L. Yingliang, S. Záliš, M. Kloz, and A. Vlček, *Journal of Physical Chemistry A* **124**, 1253–1265 (2020).